Unraveling the Degradation Mechanisms of AlGaN-Based UVC-LEDs: A Comprehensive Analysis

Pengyan Wen, Yu He, Meixin Feng, Jiahao Dong, Xinbo Zou, *Member, IEEE*, Jiaxiang Chen, Haolan Qu, Xiujian Sun, Qian Sun, and Hui Yang

***Abstract*—In the fields of medical diagnostics, virus inactivation, and air/water purification, ultraviolet-C light-emitting diodes (UVC-LEDs) have emerged as pivotal light sources, attracting substantial attention in the post-COVID-19 era. Nevertheless, their long-term reliability remains a critical area requiring further optimization. This study focuses on the degradation mechanism of AlGaN-based UVC-LEDs. Experimental results demonstrate that the aged devices exhibit a notable increase in both turn-on voltage and ideality factor. Concurrently, their electroluminescence (EL) characteristics reveal a redshift in peak emission wavelength and a significant reduction in luminescence intensity. By integrating noise analysis and cathodoluminescence (CL) characterization, we conclude that defect-related nonradiative recombination centers were generated in the n-AlGaN layer beneath the quantum wells (QWs), and these centers facilitate defect-mediated carrier tunneling, contributing to the observed performance degradation. This research provides valuable insights to guide the subsequent design and development of high-reliability UVC-LEDs.**

***Index Terms*—Cathodoluminescence (CL), degradation mechanism, electroluminescence (EL), noise analysis, ultraviolet-C light-emitting diodes (UVC-LEDs).**

Received 20 January 2026; revised 2 March 2026; accepted 25 March 2026. Date of publication 6 April 2026; date of current version 24 April 2026. This work was supported in part by the Key Research and Development Program of Jiangsu Province under Grant BE2023018-2, in part by the Natural Science Foundation of Shanghai under Grant 24ZR1470700, and in part by the Fundamental Research Funds for the Central Universities under Grant 22120250234. The review of this article was arranged by Editor J. Zhang. *(Corresponding authors: Meixin Feng; Qian Sun.)*

Pengyan Wen is with the College of Electronics and Information Engineering, Shanghai Institute of Intelligent Science and Technology, Tongji University, Shanghai 201804, China (e-mail: pywen@tongji.edu.cn).

Yu He and Jiahao Dong are with the College of Electronics and Information Engineering, Tongji University, Shanghai 201804, China.

Meixin Feng, Xiujian Sun, Qian Sun, and Hui Yang are with the Key Laboratory of Semiconductor Display Materials and Chips, Suzhou Institute of Nano-Tech and Nano-Bionics (SINANO), Chinese Academy of Sciences (CAS), Suzhou 215123, China (e-mail: mxfeng2011@sinano.ac.cn; qsun2011@sinano.ac.cn).

Xinbo Zou, Jiaxiang Chen, and Haolan Qu are with the School of Information Science and Technology, ShanghaiTech University, Shanghai 201210, China.

Digital Object Identifier 10.1109/TED.2026.3679316

I. Introduction

ULTRAVIOLET-C light-emitting diodes (UVC-LEDs), emitting light in the wavelength range of 200–280 nm, are being widely used in virus inactivation [1], [2], medical diagnostics [3], [4], biochemical detection [5], and water purification [6]. Through sustained research on materials and device architectures, significant progress has been achieved in improving their efficiency [7] and tuning their emission wavelength [8]. Nevertheless, the lifetime of UVC-LEDs remains limited to a few thousand hours [9], [10], and challenges persist regarding their long-term reliability and performance stability [11], [12], [13].

Typical UVC-LED degradation processes include p-contact degradation, as well as a reduction in efficiency and output power. Intrinsic defects—such as threading dislocations [14], point defects [e.g., C_N complexes, Ga vacancies (V_{Ga}), or N vacancies (V_N)] [15]—and their propagation during device operations are generally recognized as the primary factors contributing to degradation [16], [17], [18]. However, degradation mechanisms vary substantially depending on the specific device structure and emission wavelength.

To contribute to this field of research, we present an analysis of the degradation mechanisms of AlGaN-based UVC-LEDs with an electroluminescence (EL) peak wavelength of ~275 nm. This analysis is based on the combination of electrical, optical, noise, and cathodoluminescence (CL) characterization techniques. Specifically, we observed increases in the operating voltage, turn-on voltage, leakage current, and ideality factor of aged devices. Concurrently, a significant decrease in emission intensity (consistent with reduced efficiency) and a redshift in the emission peak wavelength were detected. By integrating these observations with noise analysis and CL characterization, we attribute the observed degradation to the generation of defects in both the active region and the n-AlGaN layer.

II. Experiments

The UVC-LEDs investigated in this study were grown on the *c* plane sapphire substrate via metal-organic chemical vapor deposition (MOCVD) [16]. The epitaxial structure was fabricated as follows. First, a 4-μm-thick AlN buffer layer was deposited on the substrate, followed by a 300-nm-thick $AlN/Al_{0.85}Ga_{0.15}N$ superlattice transition layer. A 3-μm-thick AlGaN film with step-graded Al mole fractions (ranging from

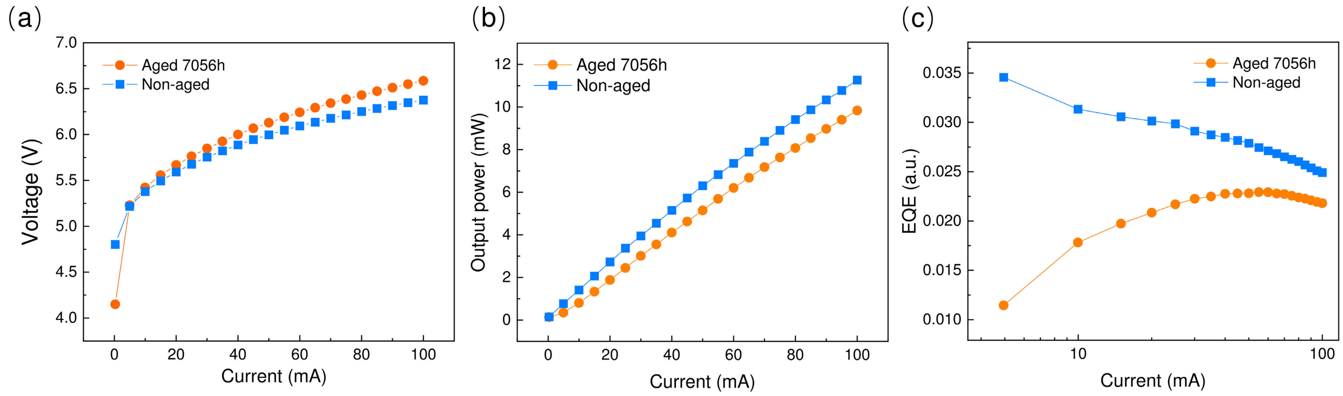

Fig. 1. Typical degradation data of the investigated LEDs. (a) *I–V* curves. (b) Output power. (c) EQE of nonaged and aged LEDs after 7056 h.

0.75 to 0.5) was then grown atop the transition layer. The active region consists of five pairs of $Al_{0.4}Ga_{0.6}N/Al_{0.52}Ga_{0.48}N$ multiquantum wells (MQWs). For the p-type region, the structure includes a 25-nm-thick Mg-doped $Al_{0.6}Ga_{0.4}N$ electron blocking layer (EBL), a 50-nm-thick p-$Al_xGa_{1-x}N$ grading layer (with Al mole fraction x decreasing from 0.4 to 0), and a 10-nm-thick p-GaN contact layer as the top layer. After epitaxial growth, the wafers were processed into chips with a size of 250 × 500 μm^2. The devices were subjected to accelerated aging at room temperature under a constant current of 100 mA (corresponding to a current density of ~200 A/cm^2) for a total duration of 7056 h. Given the excellent interdevice repeatability of devices fabricated from the same epitaxial wafer and following an identical manufacturing process, we herein present and characterize two representative device samples for comparative analysis: one subjected to 7056 h of aging and the other maintained in the as-fabricated (nonaged) state.

III. Results and Discussion

Fig. 1(a) presents the current–voltage (*I–V*) characteristics of both the as-fabricated (nonaged) and aged UVC-LEDs. The blue squares denote the *I–V* curve of the nonaged device, while the orange dots represent that of the aged device. A notable voltage increase of 0.2 V at 100 mA is observed for the aged LED compared to the nonaged counterpart. Fig. 1(b) and (c) illustrates the output power and external quantum efficiency (EQE) of the devices, respectively. Both the output power and EQE show a significant decrease after aging. For the nonaged device, EQE decreases monotonically with increasing current: the low initial defect density ensures high- and low-current EQE, while current-induced effects (quantum-confined Stark effect, Joule heating, and carrier screening) cause EQE degradation at high currents. For the aged device, EQE remains persistently low. It rises slightly at low currents (dominated by aging-induced nonradiative recombination centers) and then drops at high currents (limited by electron leakage and Auger recombination) [19], [20], [21]. ABC model analysis reveals a 13.5% increase in parameter A, accompanied by 8.2%, 6.3%, and 6.4% changes in parameters B, C, and D, respectively. This distinct parameter shift—especially the significant increase in A—identifies enhanced nonradiative recombination as the primary driver of UVC-LED performance degradation [22], [23]. All electrical and optical characterizations in Fig. 1 were performed under continuous-wave (CW) operation at room temperature and atmospheric pressure.

To extract additional insights from the *I–V* characteristics, temperature-dependent *I–V* measurements were performed on both the nonaged and aged devices. Fig. 2(a) presents the *I–V* characteristics of the nonaged device over a temperature range of 90–300 K. Analysis of the overall *I–V* curve reveals three distinct current-dominant regimes: 1) a voltage range of −5 to 2.7 V, where leakage current is governed by parallel resistance; 2) a voltage range of 2.7–4.5 V, dominated by recombination current; and 3) a voltage range of 4.5–7 V, where current is limited by series resistance. As temperature increases, both the recombination current and series resistance-dominated current increase, whereas the parallel resistance-governed leakage current remains unchanged. Fig. 2(b) shows the *I–V* characteristics of the aged LED, which exhibits a strongly temperature-sensitive current across the entire voltage range of −5 to 7 V. Furthermore, compared to the nonaged device, the leakage current of the aged device at −5 increases substantially from 1.2×10^{-7} to 1.5×10^{-5} A.

To further clarify the *I–V* behavior, the turn-on voltage and ideality factor were compared between the nonaged and aged LEDs. Fig. 2(c) plots the turn-on voltage as a function of temperature. The turn-on voltage increases with decreasing temperature, a trend primarily driven by the temperature dependence of the bandgap energy and the thermal activation of carriers. Notably, after aging, the temperature coefficient of the turn-on voltage increases from 1.6 to 3.5 mV/K.

Two distinct regions of the forward *I–V* curves were observed on both aged and nonaged devices—below the turn-on voltage and above the turn-on voltage [24], [25].

1) *Below the Turn-On Voltage:* Series resistance is negligible, so the ideality factor (n) was extracted using

$$I = I_s e^{qV/(nkT)} \tag{1}$$

where I is the current, I_s is the saturation current, q is the elementary charge, V is the voltage, k is Boltzmann's constant, and T is the absolute temperature.

2) *Above the Turn-On Voltage:* Series resistance (R_s) must be considered, so the ideality factor was calculated using

$$V = \frac{nkT}{q} \ln\left[\frac{I}{I_s} \exp\left(\frac{qIR_s}{nkT}\right)\right]. \tag{2}$$

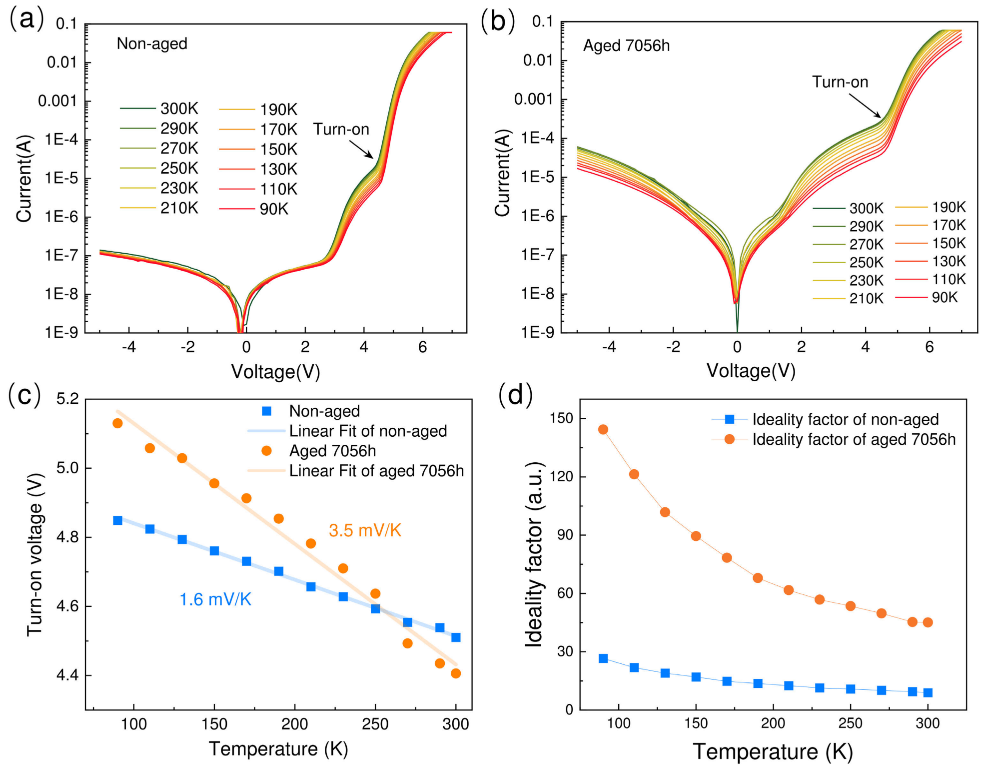

Fig. 2. *I–V* characteristics of nonaged and aged LEDs. (a) Temperature-dependent *I–V* curves of nonaged LED. (b) Temperature-dependent *I–V* curves of aged LED. (c) Temperature-dependent turn-on voltage of aged and nonaged LEDs. (d) Temperature-dependent ideality factors of aged and nonaged LEDs.

Fig. 2(d) presents the ideality factors of aged and nonaged devices derived from the *I–V* data below the turn-on voltage. For both devices, the ideality factor decreases as temperature increases—this trend arises from trap-assisted or other defect-dominant carrier transport mechanisms that are prominent at low temperatures. As the temperature rises, thermal activation enables carriers to bypass these traps, resulting in a corresponding drop in the ideality factor [26], [27]. Notably, the aged device exhibits a higher ideality factor than the nonaged device, suggesting an accumulation of defects (e.g., trap states) in the device following long-term aging [28], [29], [30].

Fig. 3 presents the typical output spectra of the UVC-LEDs as a function of drive current. Specifically, Fig. 3(a) and (b) shows the EL spectra of the nonaged and aged devices, respectively, measured under injection currents ranging from 5 to 100 mA in 5-mA increments. The insets show the EL mappings at 5 and 50 mA, revealing a significant reduction in both emission intensity and spatial homogeneity for the aged device at both current levels. Fig. 3(c) illustrates the integrated EL intensity for both devices, with the aged LED exhibiting a substantial reduction—most notably at lower injection currents. Fig. 3(d) plots the full-width at half-maximum (FWHM) and peak wavelength. The FWHM increases with injection current but remains comparable between the nonaged and aged LEDs. For both devices, the peak wavelength undergoes an initial blueshift followed by a redshift as the injection current increases from 5 to 100 mA. However, the aged LED shows a diminished blueshift at lower currents and intensified redshift at higher currents compared to the nonaged device. This behavior aligns with our previous observations on InGaN MQW degradation [31], [32], suggesting degradation within the quantum wells (QWs). In addition, the aged LED exhibits an overall redshift of approximately 0.8 nm relative to the nonaged device [33], consistent with an increase in nonradiative recombination centers.

To further investigate the nature of defects contributing to the UVC-LED degradation, we compared the current noise spectra density (S_I) of the aged and nonaged devices. The low-frequency noise measurements were conducted using an FS-Pro380 semiconductor parameter analyzer coupled with a PX500 Controller and Modular Chassis. The FS-Pro380 is integrated with a DC measurement subsystem and a low-frequency noise measurement subsystem, enabling simultaneous characterization of DC signals and low-frequency noise. The system-induced noise is approximately 10^{-28} A^2/Hz, which is negligible in comparison to the noise generated by the tested device. In addition, the device was tested in a Lakeshore cryogenic system to investigate the low-frequency noise behavior at various temperatures.

Fig. 4 presents the current noise spectra density (S_I) of the UVC-LEDs measured at fixed current levels of 1.1×10^{-5} A and 2.0×10^{-3} A, over a frequency range from 10^0 to 10^5 Hz. All curves exhibit a decreasing S_I with increasing frequency, characteristic of low-frequency 1/f noise dominated by defect-mediated carrier number fluctuations [34]. For both aged and nonaged devices, S_I is notably higher at the higher current level, which aligns with the $S_I \propto J^2$ relationship (where J is current density). This behavior arises from enhanced carrier trap interactions at elevated injection levels, as reported in the

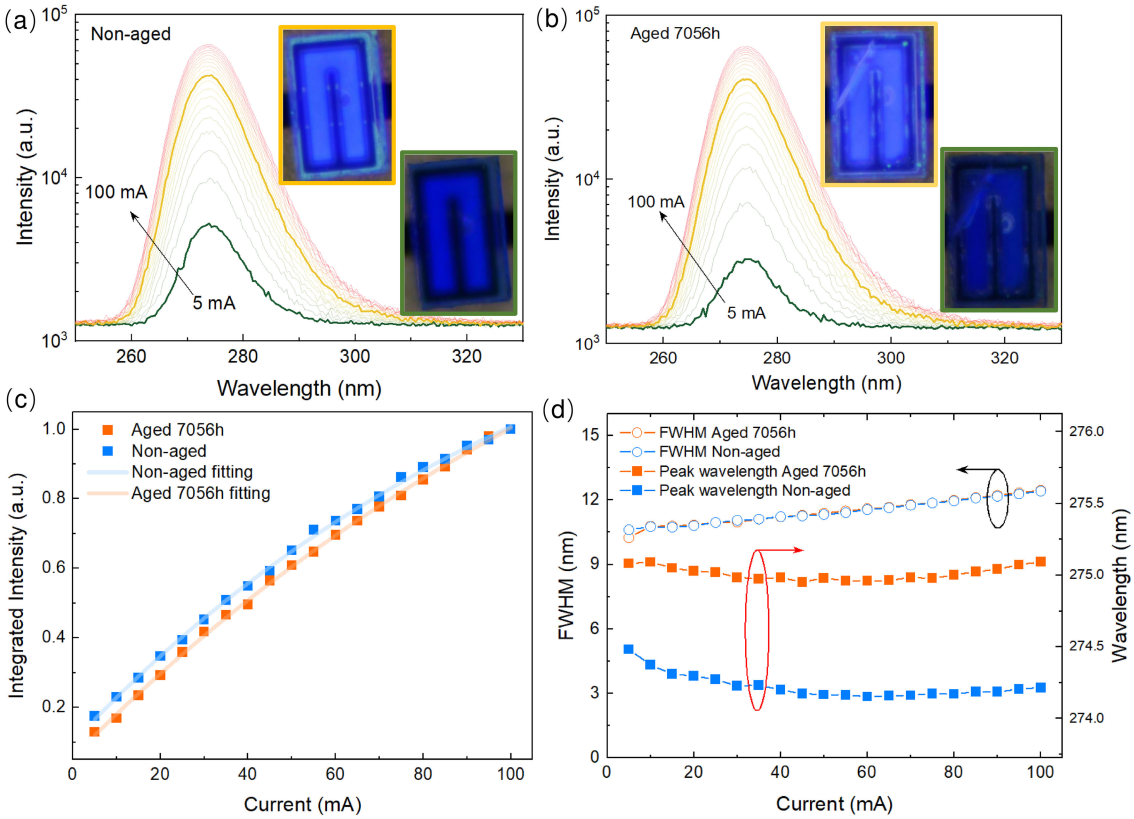

Fig. 3. Typical emission spectra from UVC-LEDs as a function of drive current. (a) EL spectra of nonaged LED under drive current from 5 to 100 mA, and the EL mapping of 5 and 50 mA in the inset. (b) EL of aged LED under drive current from 5 to 100 mA, and the EL mapping of 5 and 50 mA in the inset. (c) Integrated intensity of aged and nonaged LEDs. (d) Peak wavelength and FWHM of aged and nonaged LEDs.

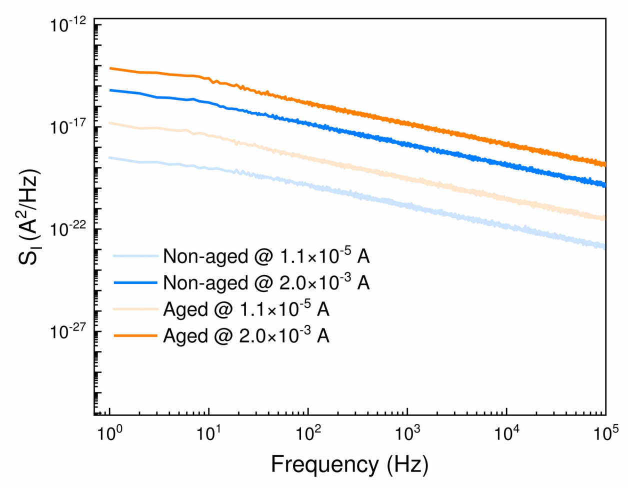

Fig. 4. Noise spectra S_I of aged and nonaged LEDs at current levels of 1.1×10^{-5} A and 2.0×10^{-3} A.

literature [35]. Moreover, the aged device displays one and two orders of magnitude higher S_I than the nonaged device at the same current level. This enhancement originates from stress-induced defect evolution in the MQW active region. These new/extended defects act as additional trap states, intensifying carrier number fluctuations. The noise results are consistent with the degradation of carrier transport uniformity in aged UVC-LEDs, suggesting a potential connection between defect dynamics and low-frequency noise behavior.

To further characterize defect-related behavior, temperature-dependent noise spectra measurements were conducted on both aged and nonaged UVC-LEDs. Fig. 5(a) and (b) displays the dependence of noise spectra density times frequency ($S_I f$) of the nonaged and aged devices, respectively. For both devices, $S_I f$ decreases with decreasing temperature—consistent with the temperature dependence of carrier-mediated noise mechanisms (e.g., generation–recombination noise) [36], [37]. Lower temperatures suppress carrier activity, thereby reducing noise magnitude. Fig. 5 presents the noise spectra times frequency $S_I f$ for the aged and nonaged LEDs, a well-established method to eliminate the influence of flicker noise on low-frequency noise analysis [38], [39]. For both devices, the magnitude of $S_I f$ decreases with decreasing temperature ranging from 1.8×10^{-13} to 2.4×10^{-16} for the nonaged device, and from 1.1×10^{-13} to 3.8×10^{-16} for the aged one, as temperature decreased from 297 to 147 K. This trend reflects weakened thermal excitation and a corresponding reduction in carrier generation–recombination activity. Noise peaks are observed in the low-frequency range (~ 10^0–10^1 Hz), which arise when the carrier relaxation time is comparable to the reciprocal of the measurement frequency [39]. A comparison of the characteristics between aged and nonaged devices reveals a significant shift in peak frequency toward higher values after aging, particularly at low temperatures. This observation indicates a reduction in the carrier trapping/detrapping lifetime [40]. Notably, the temperature-dependent trend of the noise peaks remains similar for both aged and nonaged

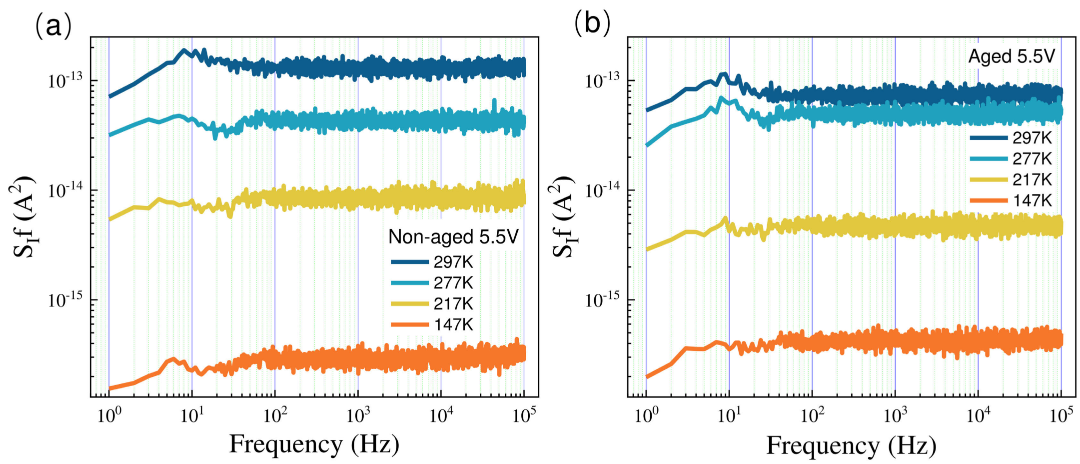

Fig. 5. Noise spectra times frequency $S_I \times f$ of (a) nonaged LED and (b) aged LED measured under 5.5 V, at various temperatures of 297, 277, 217, and 147 K.

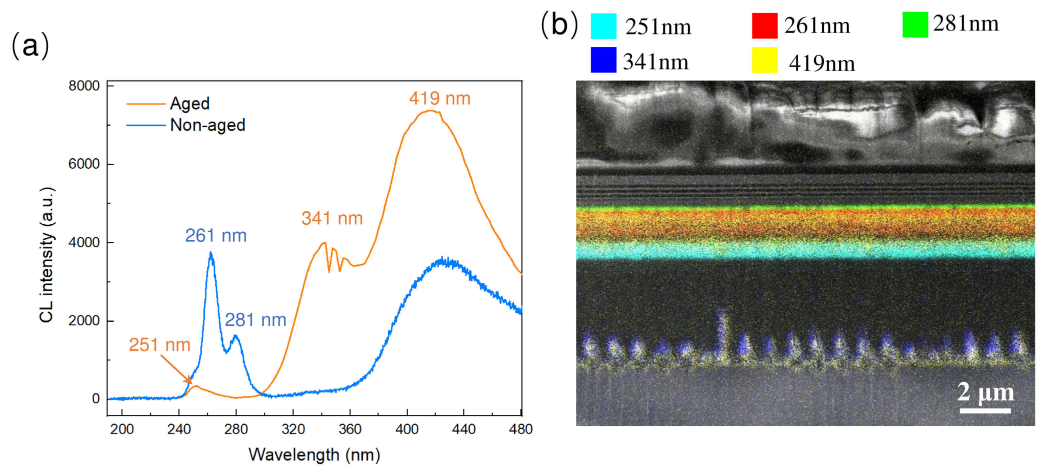

Fig. 6. CL mapping and emission spectra of UVC-LEDs. (a) CL spectra of nonaged and aged devices. (b) Overlay of cross-sectional monochromatic CL images of nonaged devices.

devices, confirming that aging enhances defect-related noise-generating processes without altering the underlying physical mechanisms responsible for the noise peaks.

To gain more insights into the spatial distribution of defects within the UVC-LED layer structure, cross-sectional CL measurements were performed on both aged and nonaged devices. The CL measurements were conducted using the SU8600/Monnac Pro, a high-resolution cold-field emission scanning electron microscope equipped with a CL detector. Fig. 6(a) shows the CL spectra of the nonaged (blue curve) and aged (orange curve) UVC-LEDs. The CL spectrum of the nonaged device exhibits three distinct emission peaks centered at 261, 281, and 419 nm. The 281-nm peak corresponds to the emission from the MQW, whereas the broad 419-nm emission arises from deep-level recombination involved in $(V_{III})^{3-}$ and V_{III} complex-related transitions of n-AlGaN layer [41]. In addition to the primary 261-nm peak, a discernible emission shoulder is observed at 251 nm, originating from the band-to-band transition of the underlying n-AlGaN and the hillock top edges, according to our previous studies [16]. When comparing the CL spectra of the aged device with the nonaged counterpart, the QW-associated emission at 281 nm is no longer detectable. Conversely, the deep-level emission at 419 nm is notably enhanced: the integrated intensity ratio from the 240–300-nm (QW-related) peak to the 370–480-nm (defect-related) peak decreases from 0.258 (nonaged device) to 0.014 (aged device). In addition, distinct peaks at 251 and 341 nm are observed in the CL spectra of the aged device. To spatially localize these emission features, monochromatic CL imaging was performed, with the overlay of key emission signals shown in Fig. 6(b). This overlay confirms that the 419-nm emission primarily originates from the n-AlGaN layers beneath the QWs. These observations indicate that the long-term aging process introduces new defects in the n-AlGaN layer; these defects act as nonradiative recombination centers, diverting charge carriers that would otherwise contribute to UV emission from the QWs. This carrier loss ultimately leads to the observed decrease in device output efficiency.

IV. Conclusion

In this study, we investigated the degradation mechanisms of AlGaN-based UVC-LEDs (with EL peak wavelength of

~275 nm) via a comprehensive combination of characterizations, including electrical measurements, optical analysis, noise spectroscopy, and CL imaging. We observe an increase in turn-on voltage, ideality factor, and leakage current. Further temperature-dependent measurements revealed enhanced temperature sensitivity of leakage current, alongside a steeper temperature dependence of turn-on voltage after aging. Noise spectra further revealed that aging intensifies defect-mediated carrier generation–recombination processes without altering the fundamental physical mechanism responsible for noise generation. Cross-sectional CL analysis provided critical spatial insights: defects generated during aging are predominantly localized in the n-AlGaN layers. These defects act as nonradiative recombination centers, diverting charge carriers away from the QW region and thereby reducing UV emission efficiency. These findings provide crucial guidance for the design and development of high-reliability UVC-LEDs, emphasizing the need to mitigate defect formation not only in the active region but also in the surrounding n-AlGaN layers to preserve device performance during long-term operation.

References

[1] H. Inagaki, A. Saito, H. Sugiyama, T. Okabayashi, and S. Fujimoto, "Rapid inactivation of SARA-CoV-2 with deep-UV LED irradiation," *Emerg. Microbes Infections*, vol. 9, pp. 1744–1747, Jan. 2020.

[2] S. Liu et al., "Sec-eliminating the SARS-CoV-2 by AlGaN based high power deep ultraviolet light source," *Adv. Funct. Mater.*, vol. 31, no. 7, Feb. 2021, Art. no. 2008452.

[3] K. Sholtes and K. G. Linden, "Pulsed and continuous light UV LED: Microbial inactivation, electrical, and time efficiency," *Water Res.*, vol. 165, Nov. 2019, Art. no. 114965.

[4] H. Siwe et al., "Microbiological evaluation of ultraviolet C light-emitting diodes for disinfection of medical instruments," *Heliyon*, vol. 10, no. 17, Sep. 2024, Art. no. e37281.

[5] N. Susilo et al., "AlGaN-based deep UV LEDs grown on sputtered and high temperature annealed AlN/sapphire," *Appl. Phys. Lett.*, vol. 112, 2018, Art. no. 041110.

[6] M. Martín-Sómer, C. Pablos, C. Adán, R. van Grieken, and J. Marugán, "A review on LED technology in water photodisinfection," *Sci. Total Environ.*, vol. 885, Aug. 2023, Art. no. 163963.

[7] V. K. Sharma and H. V. Demir, "Bright future of deep-ultraviolet photonics: Emerging UVC chip-scale light-source technology platforms, benchmarking, challenges, and outlook for UV disinfection," *ACS Photon.*, vol. 9, no. 5, pp. 1513–1521, May 2022.

[8] Y. Huang, Y. Li, and D. Xiang, "A review of recent research advances on AlGaN-based deep ultraviolet light-emitting diodes," *IEEE Access*, vol. 12, pp. 131188–131204, 2024.

[9] M. Kneissl, T.-Y. Seong, J. Han, and H. Amano, "The emergence and prospects of deep-ultraviolet light-emitting diode technologies," *Nature Photon.*, vol. 13, no. 4, pp. 233–244, Apr. 2019.

[10] N. Trivellin et al., "UV-based technologies for SARS-CoV2 inactivation: Status and perspective," *Electronics*, vol. 10, p. 1703, Jul. 2021.

[11] X. Zhu et al., "Degradation analysis with characteristics and simulations of 265 nm UV-C LED," *J. Mater. Sci., Mater. Electron.*, vol. 32, no. 13, pp. 17115–17122, Jul. 2021.

[12] Z. Ma, H. Cao, S. Lin, X. Li, and L. Zhao, "Degradation and failure mechanism of AlGaN-based UVC-LEDs," *Solid-State Electron.*, vol. 156, pp. 92–96, Jun. 2019.

[13] M. Su et al., "Characterization and simulation of 280 nm UV-LED degradation," *AIP Adv.*, vol. 11, no. 3, Mar. 2021, Art. no. 035315.

[14] D. Cameron et al., "The influence of threading dislocations propagating through an AlGaN UVC LED," *Appl. Phys. Lett.*, vol. 120, no. 16, Apr. 2022, Art. no. 162101.

[15] Z. Ma et al., "The influence of point defects on AlGaN-based deep ultraviolet LEDs," *J. Alloys Compounds*, vol. 845, Dec. 2020, Art. no. 156177.

[16] J. Chen et al., "Hillock related degradation mechanism for AlGaN-based UVC LEDs," *Nanomaterials*, vol. 13, no. 9, p. 1562, May 2023.

[17] N. Roccato et al., "Modeling of the electrical characteristics and degradation mechanisms of UV-C LEDs," *IEEE Photon. J.*, vol. 16, no. 1, pp. 1–6, Feb. 2024.

[18] F. Piva et al., "Degradation of AlGaN-based UV-C SQW LEDs analyzed by means of capacitance deep-level transient spectroscopy and numerical simulations," *Appl. Phys. Lett.*, vol. 122, no. 18, May 2023, Art. no. 181102.

[19] P. Tian et al., "AlGaN ultraviolet micro-LEDs," *IEEE J. Quantum Electron.*, vol. 58, no. 4, pp. 1–14, Aug. 2022.

[20] S. Qu et al., "Efficiency droop in InGaN/GaN-based LEDs with a gradually varing In composition in each InGaN well layer," *Chin. Phys. B*, vol. 31, Jan. 2022, Art. no. 181102.

[21] Y. Chen et al., "Review on the progress of AlGaN-based ultraviolet light-emitting diodes," *Fundam. Res.*, vol. 1, no. 6, pp. 717–734, Nov. 2021.

[22] J. Gao et al., "Degradation behavior of deep ultraviolet LEDs: The role of polarization induced doping in p-AlGaN layer," *J. Phys. D, Appl. Phys.*, vol. 58, no. 26, Jun. 2025, Art. no. 265107.

[23] Y. Gu et al., "Research on degradation characteristics of 253 nm AlGaN-based micro-LEDs for charge management application," *Opt. Exp.*, vol. 33, no. 7, p. 15327, 2025.

[24] H.-J. Kim, G.-H. Ryu, W.-B. Yang, and H.-Y. Ryu, "Ideality factor of GaN-based light-emitting diodes determined by the measurement of photovoltaic characteristics," *J. Korean Phys. Soc.*, vol. 65, no. 10, pp. 1639–1643, Nov. 2014.

[25] W. Shockley, "The theory of p-n junctions in semiconductors and p-n junction transistors," *Bell Syst. Tech. J.*, vol. 28, no. 3, pp. 435–489, Jul. 1949.

[26] A. Kumar, S. Nagarajan, M. Sopanen, V. Kumar, and R. Singh, "Temperature dependent 1/fnoise characteristics of the Fe/GaN ferromagnetic Schottky barrier diode," *Semicond. Sci. Technol.*, vol. 30, no. 10, Oct. 2015, Art. no. 105022.

[27] S. Mahato, D. Biswas, L. G. Gerling, C. Voz, and J. Puigdollers, "Analysis of temperature dependent current-voltage and capacitance-voltage characteristics of an Au/V_2O_5/n-Si Schottky diode," *AIP Adv.*, vol. 7, no. 8, Aug. 2017, Art. no. 085313.

[28] A. Jayawardena and N. Narendran, "Analysis of electrical parameters of InGaN-based LED packages with aging," *Microelectron. Rel.*, vol. 66, pp. 22–31, Nov. 2016.

[29] A. S. Hedzir and N. F. Hasbullah, "A review of high ideality factor in gallium nitride-based light-emitting diode," *Semicond. Phys., Quantum Electron. Optoelectronics*, vol. 24, no. 1, pp. 83–89, Mar. 2021.

[30] Y. Liu, K. Zhang, J. Chan, S. Yeung, Z. Liu, and H.-S. Kwok, "The size and temperature effect of ideality factor in GaN/InGaN multiple quantum wells micro light emitting diodes (micro-LEDs)," in *Proc. Int. Conf. Display Technol.*, vol. 52, 2020, pp. 387–390.

[31] P. Wen, H. Xiu, S. Zhang, J. Liu, Y. Chen, and H. Yang, "Atomic-level quantum well degradation of GaN-based laser diodes investigated by atom probe tomography," *J. Appl. Phys.*, vol. 136, no. 4, Jul. 2024, Art. no. 043103.

[32] P. Wen et al., "Asymmetrical quantum well degradation of InGaN/GaN blue laser diodes characterized by photoluminescence," *Appl. Phys. Lett.*, vol. 111, no. 21, Nov. 2017, Art. no. 212102.

[33] P. Wen et al., "Investigation of InGaN/GaN laser degradation based on luminescence properties," *J. Appl. Phys.*, vol. 119, no. 21, Jun. 2016, Art. no. 203107.

[34] S. Sawyer, S. L. Rumyantsev, and M. S. Shur, "Current and optical noise of GaN/AlGaN light emitting diodes," *J. Appl. Phys.*, vol. 100, no. 3, 2006, Art. no. 034504.

[35] S. L. Rumyantsev et al., "Low-frequency noise of GaN-based ultraviolet light-emitting diodes," *J. Appl. Phys.*, vol. 97, no. 12, Jun. 2005, Art. no. 123107.

[36] V. Palenskis, J. Matukas, J. Glemža, and S. Pralgauskaitė, "Review of low-frequency noise properties of high-power white LEDs during long-term aging," *Materials*, vol. 15, no. 1, p 13, Dec. 2021.

[37] Q. Zhao, X. Lu, J. Xu, F. Yu, Z. Jincan, and J. Xu, "Research on 1/f noise degradation of GaN LED caused by γ radiation under high bias," *Semicond. Sci. Technol.*, vol. 35, no. 8, Aug. 2020, Art. no. 085012.

[38] M. Zhu et al., "Temperature-dependent electrical characteristics of neutron-irradiated GaN Schottky barrier diodes," *Microelectron. Rel.*, vol. 125, Oct. 2021, Art. no. 114345.

[39] S. Ghosh et al., "Low-frequency noise in β-$(Al_xGa_{1-x})O_3$ Schottky barrier diodes," *Appl. Phys. Lett.*, vol. 122, May 2023, Art. no. 212109.

[40] H. Qu et al., "Reliable electrical performance of β-Ga_2O_3 Schottky barrier diode at cryogenic temperatures," *J. Vac. Sci. Technol. A, Vac. Surf. Films*, vol. 42, no. 2, Mar. 2024, Art. no. 023418.

[41] N. Nepal, M. L. Nakarmi, J. Y. Lin, and H. X. Jiang, "Photoluminescence studies of impurity transitions in AlGaN alloys," *Appl. Phys. Lett.*, vol. 89, no. 9, Aug. 2006, Art. no. 092107.